Rare Metal Materials and Engineering
Volume 49, Issue 8, August 2020
Available online at www.rmme.ac.cn

Science Press

Cite this article as: Rare Metal Materials and Engineering, 2020, 49(8): 2674-2682.

ARTICLE

Thermal Process Calculation and Analysis in VPPA-MIG Hybrid Welding of Thick High-Strength Aluminum Alloy Plates

Sun Zhenbang, Han Yongquan, Du Maohua, Sun Wanli, Han Jiao

Inner Mongolia University of Technology, Hohhot 010051, China

Abstract: To further improve the numerical calculation of variable-polarity plasma arc (VPPA)-metal inert gas (MIG) welding, the heating behavior of VPPA-MIG welding was analyzed using a high-speed camera. A variable-polarity finite element model was developed and optimized for the numerical analysis of the thermal process in VPPA-MIG welding. This model incorporated the heating mode of the VPPA with its periodic variations. Moreover, in order to more accurately express the hybrid welding conditions, the coupling interaction between the two heat sources in the electrode-negative and electrode-positive phases was taken into account. Experiments were conducted to obtain weld dimensions to verify the predicted results. This simulation results show that the fusion width of the VPPA-MIG welded joint is smaller than that of the MIG welded joint, and the penetration ability of hybrid welding is also stronger. There is a conspicuous difference in the form of heat input and thermal process between VPPA-MIG and MIG welding, which directly affects the microstructure and mechanical properties of the welds. Comparing the microstructures of the VPPA-MIG and the traditional MIG welds, it is found that the swing of the hybrid arc in VPPA-MIG welding can facilitate the production of fine aluminum grains in thick aluminum alloy plates. Consequently, the hardness and tensile properties of the hybrid welded joints are significantly higher than those produced under MIG traditional welding.

Key words: aluminum alloy; hybrid welding; heat source model; microstructure; mechanical properties

Aluminum alloys have been widely applied in national defense industries, since they are light weight, highly tough, and corrosion resistant. In the structure of light-armored vehicles, high-strength aluminum alloys have become the ideal material due to their light weight and high reliability[1-4]. However, in the welding of thick high-strength aluminum alloys in armored vehicles, the oxide film of the aluminum alloy surface should be cleaned, a groove should be opened before welding, and multi-layer and multi-pass welding should be performed by metal inert gas (MIG) or double-wire MIG welding. Consequently, this would greatly increase production costs and reduce production efficiency.

With the development of welding technology, researchers have developed and investigated some highly-efficient and high-quality hybrid welding methods to achieve thick plate welding. The paraxial variable-polarity plasma arc (VPPA)-MIG welding process merges the advantages of high-energy density and cathode cleaning of VPPA welding with those of varied technological parameters and high welding efficiency of MIG welding[5-8]. The hybrid welding process can also remove oxidation films. VPPA-MIG welding is a high quality and highly efficient deep-penetration welding process, which can reduce heat input, decrease welding deformation, and reduce material consumption[9].

In 1972, Essers and Liefkens at the Philips Research Laboratories, introduced the plasma-MIG welding process[10]. Depending on the spatial location of the two welding torches, plasma-MIG welding has two hybrid forms: coaxial welding and paraxial welding. Coaxial plasma-MIG welding has already been investigated in great detail. Ono et al[11] found

Received date: August 7, 2019
Foundation item: National Natural Science Foundation of China (51665044); the Science and Technology Key Item of Inner Mongolia (201602014)
Corresponding author: Han Yongquan, Ph. D., Professor, School of Materials Science and Engineering, Inner Mongolia University of Technology, Hohhot 010051, P. R. China, Tel: 0086-471-6575752, E-mail: hanyongquan-imut@outlook.com

that coaxial plasma-gas metal arc welding (GMAW) can achieve a clean arc with low spatter and improve bead appearance. Ton[12] investigated the temperature distribution and conductivity of the arc by optical spectroscopy analysis. Hertel et al[13] established a volume-of-fluid magnetohydrodynamic arc numerical model to calculate the arc, droplet, and pool characteristics of plasma-MIG hybrid welding. Essers et al[14] determined that the arc around the tip of the welding wire tended to rotate, which led the droplet to enter into the weld pool less concentrated. Resende et al[15] claimed that the heating area of the coaxial plasma-MIG welding was wider, which indicated that a larger heating area would lead to reduced weld penetration and larger weld width. The above characteristics are not conducive to the welding of thick-plated aluminum alloys.

Paraxial VPPA-MIG welding is a deep-penetration welding technology for thick-plated aluminum alloys without forming grooves. Shao et al[16] investigated the effect of plasma-MIG welding on hot cracking susceptibility of aluminum alloys. Their results indicated that the plasma-MIG welding process could effectively reduce the thermal crack sensitivity of welded joints. Previously, our research group performed research on the heat source characteristics and numerical simulations in VPPA-MIG welding. The results indicated that the electromagnetic coupling of the hybrid arc had a compression effect on the MIG arc, while, due to the addition of VPPA, the droplet momentum in VPPA-MIG welding was larger compared to that in MIG welding[17-19]. In the numerical simulation study, a variable combined heat source model was proposed to simulate the VPPA-MIG welding process[20]. However, the interaction between the VPPA and MIG heat source was not taken into consideration in the model. In VPPA-MIG welding, the current waveform of VPPA is an AC square wave. The AC square wave magnetic field produced by VPPA leads to a different behavior in the interaction between VPPA and MIG arc during direct current electrode negative (DCEN) and direct current electrode positive (DCEP) phases. In order to quantify the thermal processes of VPPA-MIG welding more accurately, the variable heat source model still needs to be optimized. Accurate numerical calculation results can reasonably reveal the physical phenomena and thermal processes of VPPA-MIG welding and provide a prediction of the welding results[21]. In addition, there are significant differences in the form of heat input and the temperature distribution between the VPPA-MIG and the multi-pass MIG welding process. Microstructural variation occurs mainly as a result of the welding thermal process experienced by alloys during welding. In VPPA-MIG welding, the AC current waveform used in VPPA causes a periodic swing of the hybrid arc. This swing stirs the weld pool and directly affects the weld microstructure. Therefore, in order to further improve the mechanical properties of welded joints, it is necessary to explore the microstructure of thick aluminum alloy plates welded by VPPA-MIG welding.

In this research, based on an analysis of the heating behavior of VPPA-MIG welding, a variable-polarity heat source model considering the coupling interaction between the two heat sources was established in order to analyze the thermal process in hybrid welding. The effects of heat input and temperature distribution of VPPA-MIG welding on the microstructure and mechanical properties of welded joints were investigated, and the results were compared with those of traditional MIG welding. This study assists in analyzing the thermal processes and understanding the microstructure characteristics in VPPA-MIG welding of thick high-strength aluminum alloy plates.

1 Experiment

In the experiments, 7A52-T651 aluminum alloy specimens were used as the base metal. The size of the welded plates was 200 mm×80 mm×11 mm. The filler metal was ER5183 filler wire with a diameter of 1.6 mm. The chemical composition of the base metal and the welding wire is shown in Table 1.

The VPPA-MIG welding system employed in the experiments was composed of a VPPA welding power source (Magic Wave 3000), an MIG welding power source (Fronius TPS 5000), and a PLT hybrid welding torch. The distance between the VPPA and the MIG torch was 18 mm. The angle between the MIG and the VPPA torch was 16°. The distance between the plasma electrode and the workpiece was 6 mm. A schematic diagram of the VPPA-MIG welding process is shown in Fig.1. The welding speed was kept at 400 mm·min^{-1}. Pure argon gas with 40, 23, and 3.5 L·min^{-1} flux was used as the overall shielding gas, the MIG shielding gas, and the plasma gas, respectively. The electrode negative to electrode positive duration was 17 ms to 3 ms. The other welding parameters used in the experiments are listed in Table 2. Fig.2a and 2b demonstrate the groove geometry for double-pass MIG welding and one-sided VPPA-MIG welding, respectively.

Arc images were captured using a high-speed camera system. In order to verify the developed numerical model, the thermal cycles during hybrid welding were measured using an NI PXIe-4353 thermocouple input module and the LabVIEW software. The microstructures of the VPPA-MIG and MIG welded joints were characterized by optical microscopy (Axio Imager A1m). Vickers microhardness measurements in different regions of the welded joints were carried out using an FM-800

Table 1 Chemical composition of base metal and filler wire (wt%)

Material	Zn	Mg	Cu	Mn	Cr	Ti	Zr	Fe	Si	Al
7A52	4.3	2.1	0.06	0.24	0.16	0.09	0.09	0.3	0.25	Remainder
ER5183	0.25	4.95	0.01	0.75	0.12	0.15	-	0.4	0.4	Remainder

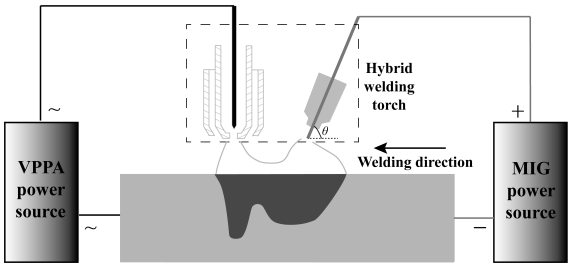

Fig.1 Schematic diagram of the VPPA-MIG welding process

hardness tester (FUTURE-TECH, Japan) under a load of 1 N. The dwell time was 10 s. The microhardness measurement locations are shown in Fig.2. The tensile strength of the VPPA-MIG and MIG welded joints was measured by transverse tensile tests at room temperature. Each test was conducted three times and the values were averaged.

2 Modelling the Heat Input of VPPA-MIG Welding

2.1 Analysis of heat source characteristics

Fig.3 displays a schematic diagram of the typical current

Table 2 Welding parameters

Process	Procedure	I_{EN}/A	I_{EP}/A	I_M/A	U_M/V	η_{EN}	η_{EP}	η_M	Total heat input/kJ·cm^{-1}
MIG	First pass	0	0	280	22.6	-	-	0.7	12.99
	Second pass	0	0	270	22.4	-	-	0.7	
VPPA-MIG	One pass	195	246	300	23.0	0.80	0.55	0.7	12.56

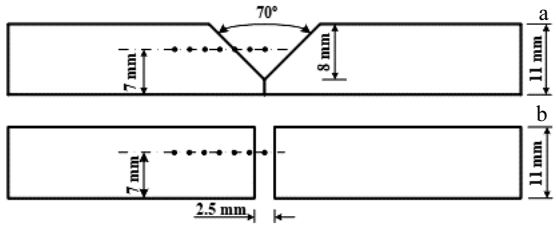

Fig.2 Groove geometry and microhardness measurement locations (represented by black dots) in MIG (a) and VPPA-MIG (b) welding

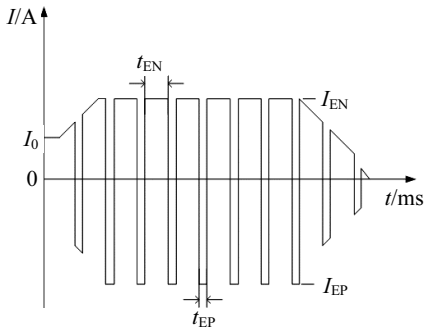

Fig.3 Typical square waveform of the VPPA welding current

waveform of VPPA welding. It can be observed that the VPPA welding current waveform has positive and negative half waves. The current amplitude and period of the positive and negative polarity phase are different. During the welding of aluminum alloys, the welding current and the power in the DCEN phase are lower than those in the DCEP phase[22-24]. The VPPA heat flux changes periodically with the duration of positive and negative polarity. The DCEN and DCEP effective power of VPPA-MIG welding can be expressed as:

$$Q_{EN}=\eta_{EN}I_{EN}U_{EN}+\eta_M I_M U_M \quad (1)$$

$$Q_{EP}=\eta_{EP}I_{EP}U_{EP}+\eta_M I_M U_M \quad (2)$$

where, η_{EN}, I_{EN}, and U_{EN} are the effective coefficient, welding current, and arc voltage of the VPPA during the DCEN phase, respectively. In addition, η_{EP}, I_{EP}, and U_{EP} are the corresponding parameters during the DCEP phase, and η_M, I_M, and U_M are the corresponding parameters of MIG.

The hybrid arc behavior captured by the high-speed camera during the two different phases is presented in Fig.4. It can be observed that during the different phases, the arc heating behavior is significantly different due to the transformation of the VPPA polarity. The arc column diameter of the VPPA during the DCEN phase is smaller than that during the DCEP phase, and the heating size during the DCEN phase is obviously smaller than that during the DCEP phase. This is due to that the cathodic pressure drop during the DCEN phase is lower compared to that during the DCEP phase, and the anode spot has adhesivity. The anode is drawn toward metals, whereas the cathode is attracted to oxide films. In the DCEN

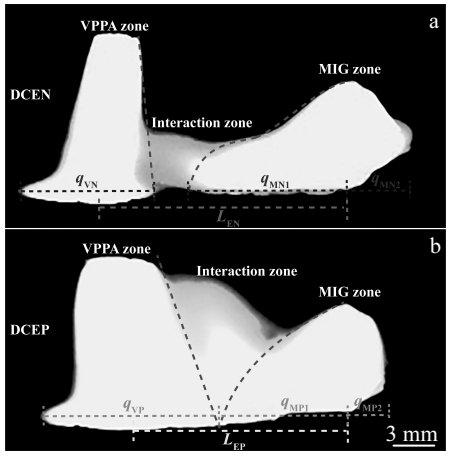

Fig.4 VPPA-MIG welding arc characteristics in the DCEN phase (a) and DCEP phase (b)

phase of VPPA-MIG welding, the VPPA is more concentrated and forms a smaller heating area, while in the DCEP phase, the arc is more dispersed and forms a larger heating area.

Some magnetic fields are induced around the VPPA and MIG arc during the VPPA-MIG welding process. The magnetic field distribution produced by the arcs changes due to the transformation of the electronic moving direction in the VPPA. The distribution of the magnetic induction lines in the VPPA-MIG welding arc is depicted in Fig.5. The current direction of VPPA and MIG during the DCEN phase is opposite and the ampere force generated by the two arcs makes the two heat sources repel each other. During the DCEP phase, the current direction of VPPA and MIG is the same and the ampere force generated by the two arcs makes the two sources attract each other. The interaction phenomenon between the two arcs can be clearly observed in Fig.4. The hybrid arc swings periodically based on the duration of the DCEN and DCEP phase. The distance between the centers of the two heat sources changes periodically due to the interaction between the two arcs in different polarity phases. The distance during the DCEN phase is 16.5 mm, whilst the distance during the DCEP phase is 14.1 mm. In addition, it can be observed in Fig.4 that the coupling interaction between the two arcs changes the heat flux distribution of the MIG arc. The coupling interaction during the DCEP phase is stronger than that during the DCEN phase. Under constant MIG power, the heat flux density in front of the MIG arc center during the DCEP phase is higher than that during the DCEN phase. The heat flux density behind the MIG arc center during the DCEP phase is lower compared to that during the DCEN phase. This is attributed to the coupling interaction between the two arcs. When the heat source model of VPPA-MIG welding was established, the coupling interaction between the two arcs was achieved by transforming the distance between the two heat sources and the heat flow distribution of the MIG heat source model in the different phases, which resulted in a more accurate calculation of the thermal process during VPPA-MIG welding.

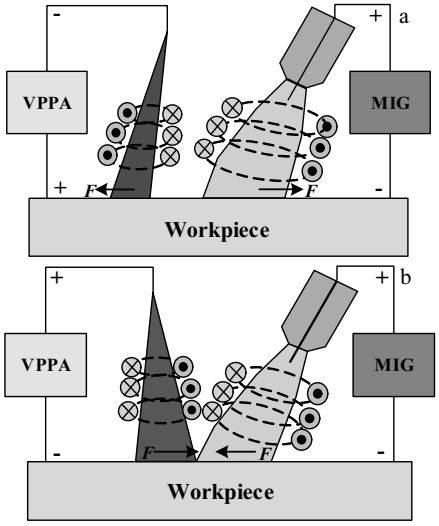

Fig.5 Magnetic field distribution of the VPPA-MIG arc in the DCEN phase (a) and DCEP phase (b)

2.2 Models of heat sources

A three-dimensional conical Gaussian heat source model was chosen for the numerical analysis of plasma arc welding. However, the power and heating area of the VPPA are different in the different phases during VPPA-MIG welding. Based on the analysis of the VPPA-MIG welding heat source characteristics, the VPPA was modeled as two three-dimensional conical Gaussian heat sources, with different heating volumes and power, which corresponded to the DCEN and DCEP heat input. Furthermore, the coupling interaction is different between the VPPA and the MIG heat source in the DCEN and the DCEP phase during hybrid welding. The heating distance between the two heat sources changes periodically with the alternation of the positive and negative polarities, due to the different ampere forces generated by the VPPA and MIG arcs during the different phases. In order to accurately describe this coupling interaction between the VPPA and MIG heat sources, the variable heat source model was modified to express the change of the heat source distance due to the interaction between the two arcs. The heat flow distribution of the developed variable heat source model is expressed by:

$$q_{\mathrm{VN}}(r_{\mathrm{N}},z)=\frac{9\eta_{\mathrm{EN}}U_{\mathrm{EN}}I_{\mathrm{EN}}\mathrm{e}^3}{\pi H_1(\mathrm{e}^3-1)(r_{\mathrm{e1}}^2+r_{\mathrm{e1}}r_{\mathrm{i1}}+r_{\mathrm{i1}}^2)}\exp(-\frac{3r_{\mathrm{N}}^2}{r_{01}^2})$$

$$r_{\mathrm{N}}=\sqrt{x^2+(y-L_{\mathrm{EN}})^2}\ \ (0<t\le t_{\mathrm{EN}}) \tag{3}$$

$$q_{\mathrm{VP}}(r_{\mathrm{p}},z)=\frac{9\eta_{\mathrm{EP}}U_{\mathrm{EP}}I_{\mathrm{EP}}\mathrm{e}^3}{\pi H_2(\mathrm{e}^3-1)(r_{\mathrm{e2}}^2+r_{\mathrm{e2}}r_{\mathrm{i2}}+r_{\mathrm{i2}}^2)}\exp(-\frac{3r_{\mathrm{p}}^2}{r_{02}^2})$$

$$r_{\mathrm{P}}=\sqrt{x^2+(y-L_{\mathrm{EP}})^2}\ \ (t_{\mathrm{EN}}<t\le t_{\mathrm{EP}}) \tag{4}$$

where, (H_1, r_{e1}, r_{i1}, r_{01}) and (H_2, r_{e2}, r_{i2}, r_{02}) are the distribution parameters for the DCEN and DCEP duration, respectively, and L_{EN} and L_{EP} are the distance between the heat sources in the DCEN and DCEP phases, respectively. t_{EN} (17 ms) and t_{EP} (3 ms) are the DCEN and DCEN time, respectively.

In order to simplify the numerical solution, the MIG arc heat input and droplet heat enthalpy in the numerical analysis of MIG welding were treated as a classic double-ellipsoidal heat source model[25]. The change of VPPA current has certain effect on MIG heat flux distribution during hybrid welding. The heat flux density in front of the MIG arc center during the DCEP phase is higher compared to that during the DCEN phase, due to the coupling interaction between the two arcs. The coupling effect on the MIG heat source was achieved through the transformation of the heat flux distribution of the front and rear ellipsoid in the DCEN and DCEP phases. Two double-ellipsoidal heat sources with different heat flux

distribution in the front and rear ellipsoid were established in order to accurately express the form of heat input in VPPA-MIG welding. The heat density distribution of the modified double-ellipsoid heat source can be written as:

$$q_{\mathrm{MN}}(x,y,z)=\begin{cases}\dfrac{6\sqrt{3}f_{\mathrm{NF}}\eta_{\mathrm{M}}U_{\mathrm{M}}I_{\mathrm{M}}}{a_{\mathrm{NF}}bc\pi\sqrt{\pi}}\exp\left[-\dfrac{3x^2}{a_{\mathrm{NF}}^2}-\dfrac{3y^2}{b^2}-\dfrac{3z^2}{c^2}\right], & (y\geq 0)\\ \dfrac{6\sqrt{3}f_{\mathrm{NR}}\eta_{\mathrm{M}}U_{\mathrm{M}}I_{\mathrm{M}}}{a_{\mathrm{NR}}bc\pi\sqrt{\pi}}\exp\left[-\dfrac{3x^2}{a_{\mathrm{NR}}^2}-\dfrac{3y^2}{b^2}-\dfrac{3z^2}{c^2}\right], & (y<0)\end{cases} \quad (0<t\leq t_{\mathrm{EN}}) \tag{5}$$

$$q_{\mathrm{MP}}(x,y,z)=\begin{cases}\dfrac{6\sqrt{3}f_{\mathrm{PF}}\eta_{\mathrm{M}}U_{\mathrm{M}}I_{\mathrm{M}}}{a_{\mathrm{PF}}bc\pi\sqrt{\pi}}\exp\left[-\dfrac{3x^2}{a_{\mathrm{PF}}^2}-\dfrac{3y^2}{b^2}-\dfrac{3z^2}{c^2}\right], & (y\geq 0)\\ \dfrac{6\sqrt{3}f_{\mathrm{PR}}\eta_{\mathrm{M}}U_{\mathrm{M}}I_{\mathrm{M}}}{a_{\mathrm{PR}}bc\pi\sqrt{\pi}}\exp\left[-\dfrac{3x^2}{a_{\mathrm{PR}}^2}-\dfrac{3y^2}{b^2}-\dfrac{3z^2}{c^2}\right], & (y<0)\end{cases} \quad (t_{\mathrm{EN}}<t\leq t_{\mathrm{EP}}) \tag{6}$$

where, f_{NF} and f_{NR} are the front and rear distribution fractions of the heat sources during DCEN, respectively, f_{PF} and f_{PR} are the front and rear distribution fractions of the heat sources during DCEP, respectively, and a_{NF}, a_{NR}, a_{PF}, a_{PR}, b, and c are the distributed parameters of heat sources. The parameters of the heat source models in the DCEN and DCEP phases were periodically loaded at 17 and 3 ms, respectively.

2.3 Boundary conditions

In the course of numerical calculation, the heat condition equation for transient non-linear heat transfer analyses is given as follows:

$$\rho C_{\mathrm{P}}\left[\frac{\partial T}{\partial t}+(-v_0)\frac{\partial T}{\partial y}\right]=\frac{\partial}{\partial x}\left(k\frac{\partial T}{\partial x}\right)+\frac{\partial}{\partial y}\left(k\frac{\partial T}{\partial y}\right)+\frac{\partial}{\partial z}\left(k\frac{\partial T}{\partial z}\right)+q_{\mathrm{v}}+q_{\mathrm{M}} \tag{7}$$

where, ρ is the density of the base metal, C_{p} is the specific heat, v is the welding speed, k is the heat conduction coefficient, T is temperature, and q_{v} and q_{M} are the internal heat sources.

The boundary conditions are described as follows:

The initial conditions, $t=0$, $T(x,y,z,0)=T_0$ (8)

On the workpiece surface, $-k\dfrac{\partial T}{\partial z}=\alpha\left(T-T_0\right)$ (9)

where, T_0 is the ambient temperature, and α refers to the heat transfer coefficient combining the convective and radiative heat loss. Free constraints were used in numerical calculations.

3 Results and Discussion

3.1 Thermal characteristics of VPPA-MIG welding

The thermal processes of VPPA-MIG welding and double-layer MIG welding of 11-mm-thick 7A52 aluminum alloy plates were calculated by the developed variable-polarity combined heat source model, while taking into consideration the coupling interaction between the VPPA and MIG arcs. Fig.6 demonstrates the calculated and the measured weld beads of double-pass MIG welding. As it can be seen in Fig.6a and 6b, the calculated weld bead profiles of the first and the second layer of MIG welding agree well with the experimentally obtained results. Fig.7 illustrates the calculated and the measured weld beads of VPPA-MIG hybrid welding, which are also in good agreement. Table 3 lists the calculated and measured weld dimensions for different welding processes. The results indicate that the heat source models could accurately simulate both the MIG and the VPPA-MIG welding. In order to further verify the thermal process, the welding thermal cycles were measured. Fig.8 displays the calculated and the measured thermal cycles at different positions. The calculated thermal cycles agree well with the experimental measurements with regards to heating rates, peak temperatures, and cooling rates.

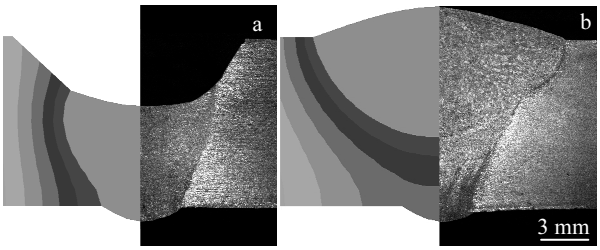

Fig.6 Comparison between the predicted and experimental cross-section in the first pass (a) and second pass (b) MIG welding

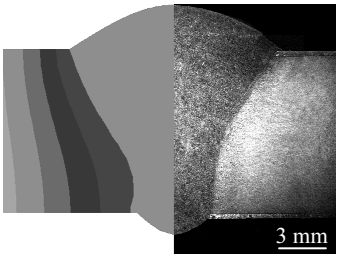

Fig.7 Comparison between the predicted and experimental cross-section in VPPA-MIG welding

Table 3 Calculated and measured dimensions of the weld bead

Process	Procedure	Weld penetration/mm		Weld width/mm	
		Calculated	Measured	Calculated	Measured
MIG	First pass	7.45	7.49	4.50	4.78
	Second pass	6.23	6.28	8.15	8.29
VPPA-MIG	One pass	12.42	12.34	6.98	7.15

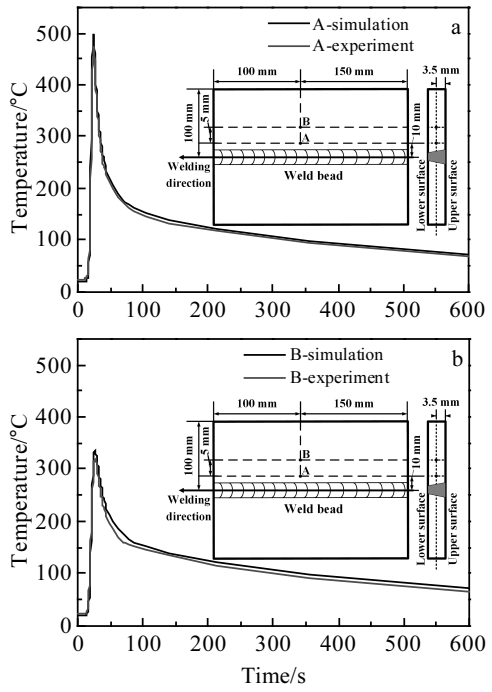

Fig.8 Calculated and experimental thermal cycles at position A (a) and position B (b)

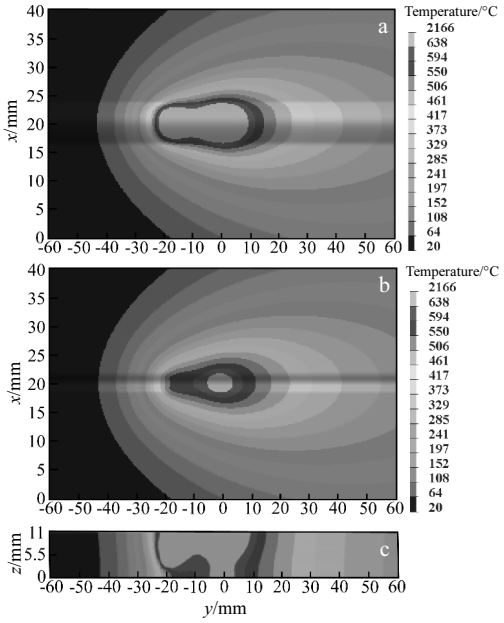

Fig.9 Predicted temperature distribution at different locations under VPPA-MIG welding: (a) top surface, (b) bottom surface, and (c) longitudinal section

Fig.9a~9c demonstrate the temperature distribution at different sections of the workpiece. It can be observed from the temperature field on the surface of the workpiece that the VPPA weld pool is coupled with the MIG weld pool in the shape of a "peanut". The elongated weld pool with a length of 31.2 mm is beneficial to the outflow of bubbles. Moreover, the pool width in front of the hybrid weld pool is narrower than that behind the weld pool. VPPA produces a smaller heating area compared to MIG. A full penetration weld seam is presented in Fig.9b. Fig.9c shows that the VPPA provides a large penetration depth which reaches 2/3 of the thickness of the aluminum alloy plates. In hybrid welding, the penetration depth is mainly determined by the VPPA, and the front of the VPPA is able to clean the oxide films of aluminum alloys. Comparing Fig.9a and Fig.9b, the weld width and the melting amount of VPPA-MIG welding are much smaller than those of MIG welding, while the hybrid welding demonstrates a stronger penetration. It is presented that VPPA-MIG welding process can join 11-mm-thick aluminum alloy plates in one pass without grooves.

3.2 Thermal characteristics of VPPA-MIG welding

According to the above research, VPPA-MIG welding needs less heat input and only one-pass welding to achieve penetration. The hybrid arc swings periodically, which has a certain influence on the microstructure and mechanical properties of welded joints. Therefore, the microstructure and mechanical properties of VPPA-MIG welded joints were investigated and compared to those of MIG welded joints.

Microphotographs of the hybrid welded joint of 7A52 aluminum alloy at different regions are presented in Fig.10. Fig.10a displays the microstructure of the fusion zone (FZ). The FZ of VPPA-MIG welding has an equiaxed grain structure with an average grain size of 43 μm and there are recrystallized grains. The microstructure of the FZ and the heat-affected zone (HAZ) are demonstrated in Fig.10b. In the HAZ, a coarse fibrillar structure in the rolling state can be observed and some uniform fine recrystallized grains are present. Fig.11a and 11b show the microstructure characteristics of the first and the second pass of the MIG welded joint, respectively. The grain size of the first pass is 140 μm and that after

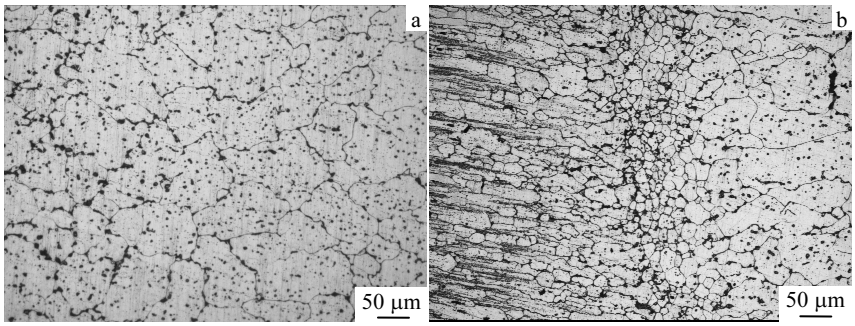

Fig.10 Microstructures at different zones of the VPPA-MIG welded joint: (a) FZ and (b) FZ+HAZ

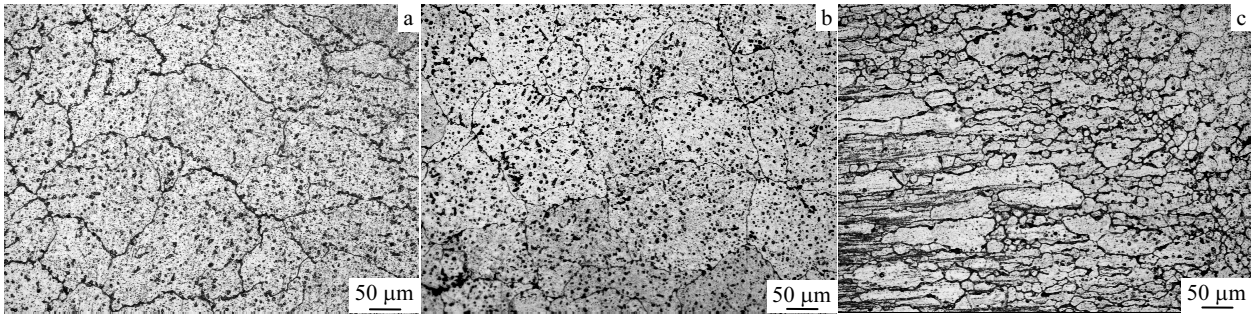

Fig.11 Microstructures of the MIG welded joint at the FZ of the first pass weld (a), the FZ of the second pass weld (b), and the FZ+HAZ (c)

the second pass is 100 μm. The grain size of the first pass weld is coarser than that of the second pass weld due to the heating action of the second pass welding. Some grains in the HAZ of the MIG welded joint are significantly coarsened. Comparing the VPPA-MIG (Fig.10) and the MIG (Fig.11) welded joints, the grain size in the FZ of the VPPA-MIG welded joint is finer than that of MIG, while the grain size in the HAZ of the VPPA-MIG welded joint is finer compared to that of MIG. The recrystallized grains, formed under MIG welding, grow at twice the grain size of those formed under hybrid welding. The grain refinement by hybrid welding is likely attributable to three reasons: (1) VPPA-MIG welding reduces the heat input to increase the cooling rate, (2) the periodic swing of the hybrid arc increases the stirring effect on the liquid metal in the weld pool, which increases the turbulence encourage the fragmentation of growing dendrites and cells, and (3) the swing of the hybrid arc between the DCEN and DCEP phase causes undercooling of the liquid metal in the weld pool. This would cause surface nucleation in the weld pool, refining the grains. A fine-grain structure can offer better mechanical properties.

The microhardness distributions in the joints welded under VPPA-MIG welding and MIG welding are presented in Fig.12. The weld hardness is composed of low microhardness in the FZ, middle microhardness in the HAZ and high microhardness

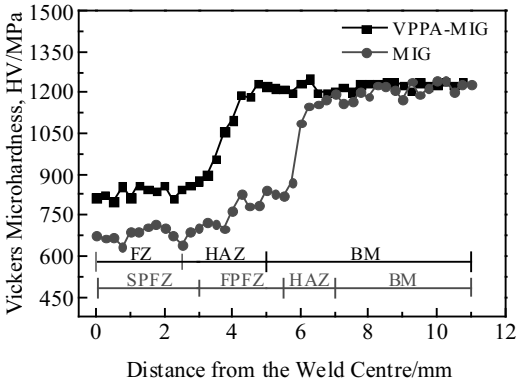

Fig.12 Microhardness distribution at different locations in the VPPA-MIG and MIG welds

in the base metal zone. The hardness (HV) of the VPPA-MIG weld in the FZ and the HAZ is about 840 and 1050 MPa, respectively. In contrast, the hardness distribution of the MIG weld demonstrates two low-microhardness zones: the first-pass fusion zone (FPFZ) and the second-pass fusion zone (SPFZ). The microhardness in the FPFZ and the SPFZ is 660 and 720 MPa, respectively. Moreover, the hardness of the MIG weld in the HAZ is about 840 MPa. The results indicate

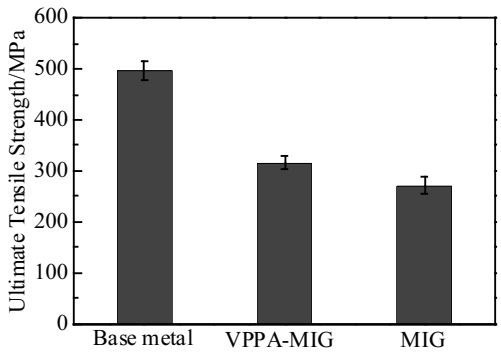

Fig.13 Tensile strength of the base metal and joints

that the hardness of the VPPA-MIG welded joint is lower than that of MIG welded joint.

Tensile tests were performed to evaluate the ultimate tensile strength of the specimens and the results are presented in Fig.13. The ultimate tensile strength of the base metal, the VPPA-MIG welded joint, and MIG welded joint was found to be 496.4, 316.2, and 271.5 MPa, respectively. The VPPA-MIG welding process can provide higher welded joint strength, equivalent to 63.7% of that of the base metal. Nevertheless, the joint efficiency of the MIG welded joint is 54.7%. The tensile strength of the VPPA-MIG welded joint is 9% higher than that produced under traditional MIG welding. This indicates that the VPPA-MIG welding process has great advantages in terms of mechanical properties.

4 Conclusions

1) Based on the experimental analysis of the coupling interaction of the VPPA-MIG welding heat source, a finite element model incorporating the coupling interaction between the VPPA and MIG heat sources was established in order to more accurately calculate the thermal process of hybrid welding.

2) The theoretically calculated weld geometry and thermal cycle show good agreement with the experimentally obtained results. The weld width of the VPPA-MIG welded joint is smaller than that resulted under MIG welding, and the penetrating ability is also much stronger. The penetration depth of VPPA-MIG welding is mainly determined by the VPPA.

3) The swing of the hybrid arc in VPPA-MIG welding facilitates the production of fine aluminum grains in thick aluminum alloy plates. Therefore, the hardness and tensile strength of the hybrid welded joints are significantly higher than those welded under traditional MIG welding. The VPPA-MIG welded joint demonstrates less tendency to soften and its joint efficiency is 63.7%, which is 9% higher than that of the MIG welded joint.

References

1 Liu S D, Yuan Y B, Li C B *et al. Metals and Materials International*[J], 2012, 18: 679
2 Xu Y Q, Tong C Y, Zhan L H *et al. Int J Adv Manuf Technol*[J], 2018, 97: 3371
3 Zhao Xiaodong, Tao Lexiao, Wang Jinliang *et al. Rare Metal Materials and Engineering*[J], 2014, 43(9): 2172 (in Chinese)
4 Zhang Yin, Song Xiping, Chang Liyan *et al. Rare Metal Materials and Engineering*[J], 2017, 46(9): 2411
5 Chen Shunjun, Xu Bin, Jiang Fan. *Acta Metallurgica Sinica*[J], 2017, 53(5): 631 (in Chinese)
6 Pan J J, Yang L J, Hu S S *et al. Int J Heat Mass Transfer*[J], 2017, 109: 1218
7 Zeng Min, Huang Junsen, Zhang Yanjie *et al. Journal of Materials Processing Technology*[J], 2017, 240: 404
8 Yi Jie, Cao Shufen, Li Luoxing *et al. Trans Nonferrous Met Soc China*[J], 2015, 25(10): 3204
9 Tong Jiahui, Han Yongquan, Hong Haitao *et al. Trans China Weld Inst*[J], 2018, 39(5): 69 (in Chinese)
10 Lee H K, Park S H, Kang C Y. *Journal of Materials Processing Tech*[J], 2015, 223: 203
11 One K, Liu Z J, Era T *et al. Weld International*[J], 2009, 23(11): 805
12 Ton H. *J Phys D: Appl Phys*[J], 1975, 8(8): 922
13 Hertel M, Füssel U, Schnick M. *Weld World*[J], 2014, 58: 85
14 Essers W G, Walter R. *Weld J*[J], 1981, 60(2): 37
15 De Resende A A, Ferraresi V A, Scotti A *et al. Welding International*[J], 2011, 25(12): 910
16 Shao Yingkai, Wang Yuxi, Yang Zhibin *et al. Acta Metallurgica Sinica*[J], 2018, 54(4): 547 (in Chinese)
17 Hong Haitao, Han Yongquan, Du Maohua *et al. Int J Adv Technol*[J], 2016, 86: 2301
18 Hong Haitao, Han Yongquan, Tong Jiahui *et al. Trans China Weld Inst*[J], 2016, 37(9): 65 (in Chinese)
19 Han Yongquan, Tong Jiahui, Hong Haitao *et al. Int J Adv Technol*[J], 2019, 101: 989 (in Chinese)
20 Sun Z B, Han Y Q, Du M H *et al. J Manuf Process*[J], 2018, 34: 688
21 Murphy A B. *Plasma Chem Plasma Proc*[J], 2015, 35: 471
22 Chen Shujun, Yan Zhaoyang, Jiang Fan *et al. Journal of Materials Processing Tech*[J], 2018, 255: 831
23 Han Yongquan, Chen Shujun, Yin Shuyan. *Trans China Weld Inst*[J], 2007, 28(12): 35
24 Sun Zhenbang, Han Yongquan, Zhang Shiquan *et al. China J Mech Eng*[J], 2016, 52(12): 46 (in Chinese)
25 Goldak J, Chakravarti A, Bibby M. *Metall Trans B*[J], 1984, 15: 299

厚板高强铝合金 VPPA-MIG 复合焊接热过程的计算与分析

孙振邦，韩永全，杜茂化，孙万利，韩　蛟
(内蒙古工业大学，内蒙古 呼和浩特 010051)

摘　要：为了进一步提高变极性等离子弧(VPPA)-金属惰性气体(MIG)复合焊接的数值计算精度，采用高速摄像机对 VPPA-MIG 焊接的热源特性进行了分析，开发并优化了一种变极性热组合源模型对 VPPA-MIG 焊接热过程进行了数值分析。该模型考虑了 VPPA 加热形式的周期性变化。此外，为了更准确地表达复合焊接，同时考虑了正、反极性两阶段复合热源的耦合作用。通过试验获得焊缝尺寸和热循环验证了数值计算结果。模拟结果表明，VPPA-MIG 复合焊的熔宽小于 MIG 焊的熔宽，复合焊接具有较强的穿透能力。VPPA-MIG 焊接与 MIG 焊接在热输入形式和热过程上存在明显差异，直接影响了焊接接头的组织与力学性能。通过对比 VPPA-MIG 焊与传统 MIG 焊的微观组织发现，VPPA-MIG 复合焊接过程中复合电弧的摆动有利于接头中产生细小均匀的晶粒。从二者焊接接头的显微硬度和抗拉强度可以看出，VPPA-MIG 复合焊接接头具有较小的软化倾向。

关键词：铝合金；复合焊；热源模型；组织；性能

作者简介：孙振邦，男，1992 年生，博士，内蒙古工业大学材料科学与工程学院，内蒙古 呼和浩特 010051， E-mail: 674984001@qq.com